Mechanisms of the Planar Growth of Lithium Metal Enabled by the 2D Lattice Confinement from a $Ti_3C_2T_x$ MXene Intermediate Layer

Di Yang, Chunyu Zhao, Ruqian Lian, Lin Yang, Yizhan Wang, Yu Gao, Xu Xiao, Yury Gogotsi,* Xudong Wang, Gang Chen, and Yingjin Wei*

The propensity of Li to form irregular and nonplanar electrodeposits has become a fundamental barrier for fabricating Li metal batteries. Here, a planar, dendrite-free Li metal growth on 2D $Ti_3C_2T_x$ MXene is reported. Ab initio calculations suggest that Li forms a hexagonal close-packed (*hcp*) layer on the surface of $Ti_3C_2T_x$ via ionic bonding and the lattice confinement. The ionic bonding weakens gradually after a few monolayers, resulting in a nanometers-thin transition region of *hcp*-Li. Above this transition region, the deposition is dominated by plating of body-centered cubic (*bcc*) Li via metallic bonding. Formation of a dense and planar Li metal anode with preferential growth along the (110) facet is explained by the lattice matching between $Ti_3C_2T_x$ and *hcp*-Li and then with *bcc*-Li, as well as preferred thermodynamic factors including the large dendrite formation energy and small migration barrier for Li. The prepared Li metal anode shows stable cycling in a wide current density range from 0.5 to 10.0 mA cm^{-2}. The LiFePO$_4$‖Li full cell fabricated with this Li metal anode exhibits only 9.5% capacity fading after 500 charge–discharge cycles at 1 C rate.

1. Introduction

Lithium-ion batteries (LIBs) have been dominating the rechargeable batteries market for nearly three decades. Despite the impressive growth of the LIBs market, further increase in energy density of LIBs is needed to meet the growing requirements for longer operation time of portable electronics and longer driving distance of electric vehicles. The availability of safe and reliable Li metal anodes would also accelerate proliferation of Li-metal batteries (LMBs) having a high energy density.[1] Nevertheless, practical application of LMBs is hindered by the safety hazards caused by uncontrolled formation of Li dendrites on the anode and low coulombic efficiency (CE) induced by the unstable interface between the metal anode and electrolyte.[2]

Deposition substrate (or current collector) is of vital importance for repeated plating/stripping of Li.[3] Copper (Cu) foil, which is used as the anode current collector of commercial LIBs, is the most economical and available substrate for Li anodes. However, it cannot be directly used in LMBs due to the formation of dendrites.[4] The micro-tips on Cu foil induce high local current density, which causes faster Li accumulation around the tips and results in the formation of dendritic nuclei,[5] which lead to concentration polarization of the electrolyte, accelerating the consumption of electrolyte and active Li. On the other hand, the uneven structure on Cu foil is often accompanied by unstable formation of a solid electrolyte interface (SEI) film, which in turn accelerates the growth of Li dendrites.[6] Compared to Cu foil, 3D-structured electrodes can provide higher surface area and reduce the local current density, thus suppressing the formation of Li dendrites.[7] Guo and co-workers prepared a 3D Cu foam as the host for Li and showed that the interconnected pores could accommodate Li without significant dendrite formation.[8] However, these 3D electrodes are delicate, and can be easily damaged during battery assembly process. In addition, the volumetric energy density of the full cells is limited due to the large volume fraction of the structured electrode. Consequently, a flat and dense Li metal anode without significant dendrite formation during long-term cycling is needed for developing practical LMBs.

D. Yang, C. Zhao, R. Lian, L. Yang, Prof. Y. Wang, Prof. Y. Gao,
Prof. G. Chen, Prof. Y. J. Wei
Key Laboratory of Physics and Technology for Advanced Batteries
(Ministry of Education)
Jilin Engineering Laboratory of New Energy Materials and Technology
College of Physics
Jilin University
Changchun 130012, China
E-mail: yjwei@jlu.edu.cn
Dr. X. Xiao, Prof. Y. Gogotsi
Department of Materials Science & Engineering, and
A. J. Drexel Nanomaterials Institute
Drexel University
Philadelphia, PA 19104, USA
E-mail: gogotsi@drexel.edu
Dr. X. Xiao
State Key Laboratory of Electronic Thin Film and Integrated Devices
School of Electronic Science and Engineering
University of Electronic Science and Technology of China
Chengdu, Sichuan 610054, China
Prof. X. Wang
Department of Materials Science and Engineering
University of Wisconsin at Madison
1509 University Avenue, Madison, WI 53706, USA

The ORCID identification number(s) for the author(s) of this article
can be found under https://doi.org/10.1002/adfm.202010987.

ADVANCED
SCIENCE NEWS
www.advancedsciencenews.com

ADVANCED
FUNCTIONAL
MATERIALS
www.afm-journal.de

The deposition of Li starts with heterogeneous nucleation on a substrate followed by homogeneous Li plating around the nuclei. To reveal the importance of the substrate on Li deposition, Cui and co-workers studied the nucleation of Li on various metal substrates.[9] It was shown that when Au and Cu co-existed in the substrate, Li tended to deposit on Au rather than on Cu. Zheng et al. reported that a conductive substrate that has a low lattice mismatch with the deposited metal layers is favorable for reversible metal plating/stripping.[10] The authors suggested that tantalum (Ta) is a good substrate for Li deposition due to the small lattice mismatch between Li and Ta. However, use of heavy and expensive metals like Au and Ta is impractical. Recently, Zhang and co-workers used the Volmer–Weber mode for vertical polycrystalline film growth to analyze Li nucleation and concluded that surface energy and migration energy of Li are two important thermodynamic factors for Li nucleation.[11] All these studies showed that the surface properties of the substrate control the Li nucleation process. Aided by this, Luo et al. modified the surface of Cu current collector with atomically distributed Zn.[12] The Zn defects lowered the interface energy between Cu current collector and Li metal, and suppressed the formation of Li dendrites. A substrate with preferred nucleation can decrease the formation of dead Li and improve the charge-discharge coulombic efficiency.[13]

Recently, 2D materials, such as graphene,[14] h-BN,[15] and MXenes,[16] have been investigated as scaffolds or substrates for Li metal anodes. Especially, 2D transition metal carbides known as MXenes have attracted attention in capacitor and battery research due to their metallic electrical conductivity,[17] exceeding that of solution processed graphene.[18] MXene aerogel,[19] MXene/graphene framework,[20] MXene-melamine foam,[21] MXene-reduced graphene oxide,[22] and pillared MXene[23] have been reported to achieve uniform and dendrite-free Li and Na deposition, which was attributed to their high conductivity, large surface area, and surface functional groups.

The 2D structure of MXenes provides a suitable substrate for deposition of alkaline metal. For example, Yang et al., reported that parallely aligned MXene nanosheets guided Li growth in horizontal direction.[24] Cao and co-workers prepared a $Ti_3C_2T_x$/carbon cloth framework to host Na metal. The deposited Na followed the laminate architecture of MXenes, resulting in planar growth of metal.[25] Despite these promising performances, the atomistic mechanism of Li and Na deposition and the reasons behind high CE and non-dendritic plating have not been well understood. Thermodynamically controlled interfacial engineering may eliminate dendrites formation,[26] but its realization requires understanding of Li nucleation and growth mechanisms. Herein, the deposition mechanism of Li on $Ti_3C_2T_x$ was comprehensively studied at the atomistic scale by ab initio calculations. Modeling was complemented by experiments using a $Ti_3C_2T_x$ MXene coated Cu foil substrate to demonstrate electrodeposition of a dense and flat Li metal anode, which was nearly dendrite-free and showed stable cycling at high current densities.

2. Results and Discussion

2.1. Preparation of the Li Metal Electrodes

A schematic diagram for the preparation of $Ti_3C_2T_x$ is presented in **Figure 1**a. First, $Ti_3C_2T_x$ was prepared by etching the Al layer from a Ti_3AlC_2 MAX phase.[27] Figure 1b shows the X-ray diffraction (XRD) patterns of Ti_3AlC_2 before and after etching. The most intense (104) reflection and other reflections of Ti_3AlC_2 disappeared, which demonstrated the formation of $Ti_3C_2T_x$. Then, a colloidal solution of $Ti_3C_2T_x$ nanosheets was prepared via exfoliation by the minimally intensive layer delamination (MILD) method.[27] The nanosheets structure of $Ti_3C_2T_x$ was confirmed by transmission electron microscopy

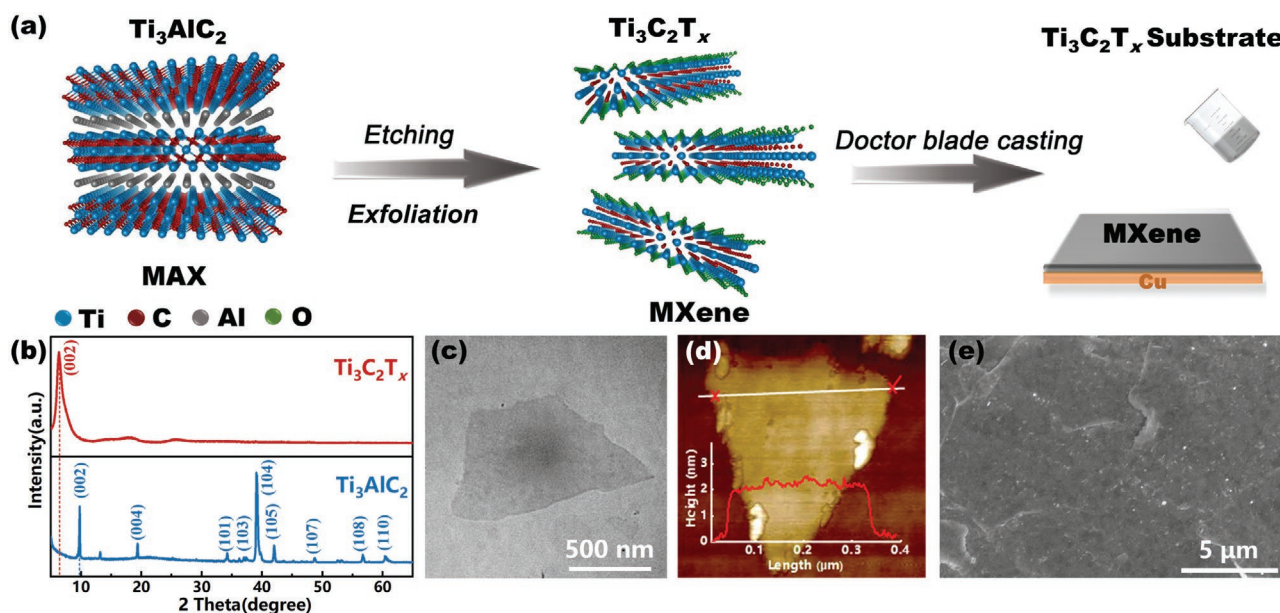**Figure 1.** Characterizations of the $Ti_3C_2T_x$ substrate. a) Schematic of preparation of the $Ti_3C_2T_x$ substrate. b) XRD patterns of Ti_3AlC_2 and $Ti_3C_2T_x$. c) TEM image and d) AFM image of the $Ti_3C_2T_x$ nanosheets. e) SEM image of the $Ti_3C_2T_x$ substrate.

**ADVANCED
SCIENCE NEWS**
www.advancedsciencenews.com

**ADVANCED
FUNCTIONAL
MATERIALS**
www.afm-journal.de

(TEM, Figure 1c) and scanning electron microscopy (SEM, Figure S1, Supporting Information). The thickness of the $Ti_3C_2T_x$ nanosheets was measured by atomic force microscopy (AFM, Figure 1d) to be about 1.8 nm in average. These characterizations demonstrated that primarily single-layered $Ti_3C_2T_x$ nanosheets were produced. X-ray photoelectron spectroscopy (XPS) confirmed the presence of O (61%), OH (34%) and F (5%) functional groups on Ti_3C_2, where O was the dominant one (Figure S2, Supporting Information). Elemental mappings confirmed the even distribution of O and F in the Ti_3C_2 matrix (Figure S3, Supporting Information). Afterwards, the slurry of delaminated $Ti_3C_2T_x$ nanosheets was casted onto a commercial Cu foil current collector by doctor blade to obtain the $Ti_3C_2T_x$ substrate. The $Ti_3C_2T_x$ coating layer had a thickness of ca. 14 μm. The excessive thickness of MXene was used to prevent any possible contact of Li with Cu in this initial study, but submicrometer-thick coatings can be deposited or free-standing MXene films of a few micrometers in thickness can be used in functioning batteries.[18] SEM showed that the surface of $Ti_3C_2T_x$ substrate was nearly flat (Figure 1e). Moreover, AFM confirmed that the $Ti_3C_2T_x$ substrate had a surface roughness similar to the Cu foil (S_a = 143 and 88 nm, respectively), which provided a prerequisite for subsequent comparison study (Figure S4, Supporting Information).

Electrodeposition was performed on the $Ti_3C_2T_x$ and Cu substrates using a 1 M $LiPF_6$ electrolyte in ethylene carbonate (EC) and diethyl carbonate (DEC) with a 1:1 volume ratio. Hereafter, the Li electrodes prepared on Cu and $Ti_3C_2T_x$ are named as Li–Cu and Li-$Ti_3C_2T_x$, respectively. All the cells were first discharged to 0.1 V, and then discharged at a constant current to deposit a fixed capacity. As shown in Figure S5, Supporting Information, the voltage of the Cu∥Li cell quickly dropped to −0.119 V at the beginning of deposition. The $Ti_3C_2T_x$∥Li cell showed a declining voltage profile in the initial deposition process, followed by a flat plateau at −0.031 V. Generally, the discharge curve for Li deposition has three typical potentials (inset of Figure S5, Supporting Information): tip potential (μ_{tip}), nucleation overpotential (μ_{nuc}) and mass-transfer controlled potential (μ_{mtc}).[28] The μ_{nuc} of $Ti_3C_2T_x$ (40.0 mV) was much lower than that of Cu (61.6 mV), which suggested that the $Ti_3C_2T_x$ substrate was more favorable for nucleation of Li.[29] A schematic illustration of Li deposition on Cu and $Ti_3C_2T_x$ is presented in Figures 2a,n, respectively. In addition, the morphological evolution of the electrodes with the areal capacity increased from 0.2 to 5.0 mA h cm^{-2} was characterized by SEM (Figure 2b–d, h–j). The two substrates showed very different Li deposition behaviors. Initially, a small number of needlelike dendrites appeared on the Cu foil (Figure 2b), and kept growing with the deposition
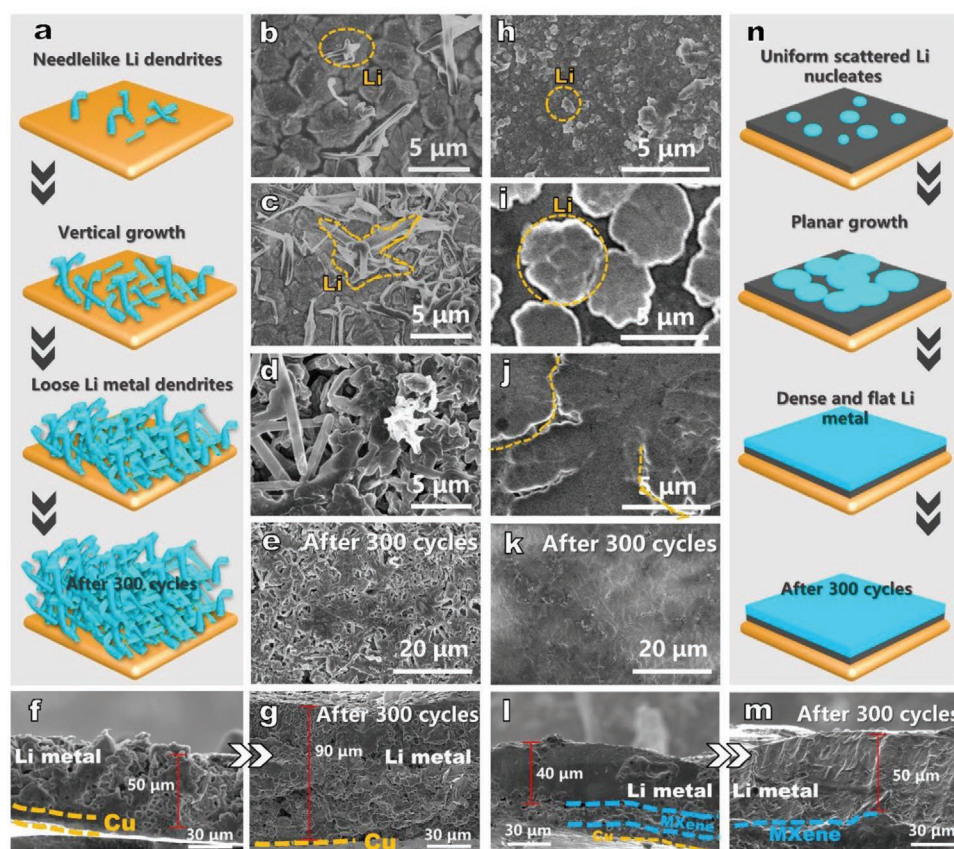

Figure 2. Morphological evolution and schematic illustration of Li deposition. Schematic illustration of Li deposition on a) Cu foil and n) $Ti_3C_2T_x$ substrate. Top-view SEM images of the Li–Cu electrodes with a capacity of b) 0.2, c) 2.0, and d) 5.0 mA h cm^{-2}. Top-view SEM images of the Li-$Ti_3C_2T_x$ electrodes with a capacity of h) 0.2, i) 2.0, and j) 5.0 mA h cm^{-2}. Cross-sectional SEM images of f) Li–Cu and l) Li-$Ti_3C_2T_x$ with a capacity of 5.0 mA h cm^{-2}. Top-view SEM images of e) Li–Cu and k) Li-$Ti_3C_2T_x$ electrodes after 300 cycles. Cross-sectional SEM images of g) Li–Cu and m) Li-$Ti_3C_2T_x$ electrodes after 300 cycles.

**ADVANCED
SCIENCE NEWS**
www.advancedsciencenews.com

**ADVANCED
FUNCTIONAL
MATERIALS**
www.afm-journal.de

capacity increased to 2.0 mA h cm^{-2} (Figure 2c). This indicated that Li metal had a tendency to grow along the dendrites on Cu. When the deposition capacity reached 5.0 mA h cm^{-2}, the Cu foil was covered by massive Li dendrites (Figure 2d). From the cross-sectional SEM image, it is found that the Li deposit on Cu foil reached about 50 µm in thickness and composed of loose dendrites (Figure 2f). Unlike the dendritic Li growth on the Cu foil, planar and uniform Li growth was observed on the Ti$_3$C$_2$T$_x$ substrate. SEM images showed that the Li deposition on Ti$_3$C$_2$T$_x$ can be divided into two stages. The first one was heterogeneous nucleation forming Li nucleates with a diameter of ca. 0.5 µm on the surface of Ti$_3$C$_2$T$_x$ (Figure 2h). With continuous deposition, Li metal expanded horizontally around the nucleates, forming smooth plates with diameter of ≈5.0 µm (Figure 2i). Next, homogeneous deposition of Li took place on these Li plates, forming a uniform and continuous Li film on the Ti$_3$C$_2$T$_x$ substrate (Figure 2j). Cross-sectional SEM of the final electrode showed a Li/Ti$_3$C$_2$T$_x$/Cu three-layer structure from top to the bottom (Figure 2l). In the elemental mapping image (Figure S6, Supporting Information), a clear boundary can be seen between the Li film and the Ti$_3$C$_2$T$_x$ coating, which demonstrated that most of Li were deposited on the surface of Ti$_3$C$_2$T$_x$ forming a metallic Li film. However, it could not be excluded that a small fraction of Li (0.25 mA h cm^{-2}, according to Figure S5, Supporting Information) was stored in the Ti$_3$C$_2$T$_x$ layer before the plating process. This MXene-related capacity is important for the formation of a high-quality Li anode, which will be explained in detail in the following section. Besides, it was noticed that the Li film formed on Ti$_3$C$_2$T$_x$ was thinner (≈40 µm) than that on the Cu foil, which demonstrated that a denser Li electrode was prepared on the Ti$_3$C$_2$T$_x$ substrate.

2.2. Ab Initio Calculations

Ab initio calculations were conducted to study the deposition of Li on Ti$_3$C$_2$T$_x$ at the atomistic scale. We first calculated the binding energies (E_{ad}) of Li on Ti$_3$C$_2$T$_x$ with different terminating groups (T = O, F, OH). Results showed that Li could not be adsorbed on OH-terminated Ti$_3$C$_2$ due to a positive E_{ad} of 0.48 eV, but it can be adsorbed on O- and F-terminated Ti$_3$C$_2$ with a negative E_{ad} of −0.41 and −1.47 eV, respectively, which were consistent with the past report.[30] Close observation of the adsorption structures showed that Li reacted with the surface F to form LiF (Figure S7, Supporting Information), which is known as a component of SEI.[24] In comparison, the O termination remained stable during Li adsorption and did not form a separate Li$_2$O phase with Li (Figure S7, Supporting Information). This showed that the Li deposition on MXenes has a strong selectivity towards terminating groups. In all the three terminating groups, OH does not allow Li deposition; F will be quickly consumed to form LiF during initial Li deposition, while only O can be stably retained during Li deposition. Accordingly, the subsequent calculations were only conducted on O-terminated Ti$_3$C$_2$T$_x$, Ti$_3$C$_2$O$_2$ for simplicity. Considering that the dominant functional group of the as-prepared Ti$_3$C$_2$T$_x$ was O, the calculation results can reasonably explain the experimental findings reported in this work. It is also important to note that OH groups can be transformed into O by heat

treatment and Ti$_3$C$_2$ with very little or no F terminating groups can be produced by modifying the synthesis process.[31]

Following we present a detailed comparison study of the Li deposition properties on Cu and Ti$_3$C$_2$O$_2$ substrates. From the top view image of Cu, it is seen that the Cu atoms form a cubic structure (**Figure 3**a). Ti$_3$C$_2$O$_2$ has a hexagonal unit cell constructed by Ti and C layers stacked in a sequence of Ti-C-Ti-C-Ti, with all of the O terminating group located at the hollow site above Ti (Figure 3c). When Li deposited on Cu, the first layer of Li formed above the center of four Cu atoms (A site). Then the second layer of Li deposited above the center of four Li atoms (B site). Following this way, Li deposited on the Cu substrate with a ···AB··· stacking (Figure 3a). For the Ti$_3$C$_2$O$_2$ substrate, all of the Li atoms deposited above the Ti$_3$C$_2$O$_2$ surface. In detail (Figure S8, Supporting Information), Li first deposited at the A' sites (above the C atom) forming a hexagonal layer. After all the A' sites were covered by Li, the subsequent Li atoms deposited at the B' sites (above the O atom) forming a new hexagonal layer. As a result, the layer-by-layer Li deposition on Ti$_3$C$_2$O$_2$ also followed the ···AB··· stacking (Figure 3c). However, due to the different surface atomic arrangements of Cu and Ti$_3$C$_2$O$_2$, the Li stacking structures on the two substrates were completely different. The Li atoms formed a body-centered cubic (*bcc*) structure on the Cu substrate with a coordination number of 8, which was the same as that of bulk Li metal, while a hexagonal close-packed (*hcp*) Li stacking with a coordination number of 6 was obtained on the hexagonal lattice of Ti$_3$C$_2$O$_2$.

Figures 3b,d show the E_{ad} of Li on Cu and Ti$_3$C$_2$O$_2$ substrates, respectively, as a function of number of deposition layer (*n*). Ti$_3$C$_2$O$_2$ showed a much larger initial E_{ad} than Cu, being −1.47 and −0.80 eV, respectively. The difference in E_{ad} between the first and second Li layers of Ti$_3$C$_2$O$_2$ (Δ = 0.76 eV) was nearly three times that of Cu (Δ = 0.24 eV). The larger energy difference of Ti$_3$C$_2$O$_2$ indicated that a new *hcp*-Li layer cannot be formed until the underlying layer is fully covered by Li. Electron density mapping and Bader charge analysis of bonding between the substrate and Li layers showed that the deposited Li atoms can only form a Li−Cu metallic bond with the Cu substrate. This is consistent with the experimental results in Figure S5, Supporting Information, which showed that the deposition voltage abruptly dropped to ≈0 V in the beginning of deposition, which is a characteristic of metal plating process. However, the lower electronegativity of Li (0.98) than that of Cu (1.90) caused the transfer of some electrons from the Li layer to the Cu substrate, as detected by the electron density mapping of the Li−Cu system (**Figure 4**a). This short-range interaction weakened rapidly with increasing thickness of the deposit, showing a sharp decline in charge transfer after three Li layers, as shown in Figure 4c. For the Li-Ti$_3$C$_2$O$_2$ system, a region with a low electron density was observed between the surface O and the first Li layer (Figure 4b), corresponding to a significant electron transfer (0.77 e atom^{-1}, Figure 4c) from Li to O. This indicates that the initially deposited Li interacted with the Ti$_3$C$_2$O$_2$ substrate via ionic bonding. The charge transfer number gradually decreased with increasing number of layers. When the deposition exceeded eight Li layers, only 0.07 e atom^{-1} was transferred from Li to the Ti$_3$C$_2$O$_2$ substrate. In addition, the electron density mapping showed a uniform
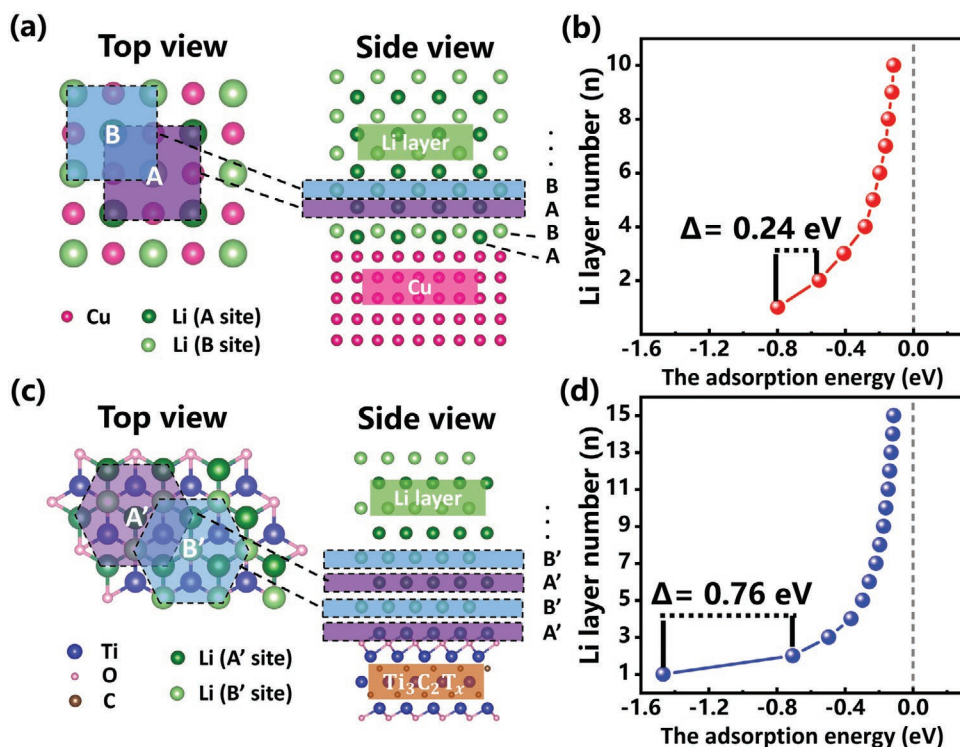
Figure 3. Theoretical modeling of Li deposition on Cu and $Ti_3C_2T_x$. Top and side views of Li deposition sites on a) Cu and c) $Ti_3C_2T_x$. Adsorption energy of Li on b) Cu and d) $Ti_3C_2T_x$.

electron distribution in the newly formed Li layer, which indicated formation of metallic Li−Li bond. In the electrodeposition experiment (Figure S5, Supporting Information), the initial decline in the voltage profile was due to the ionic interaction between Li and $Ti_3C_2O_2$. Afterwards, a long and flat voltage plateau was observed at ≈0 V, which was attributed to the plating of Li metal.

In order to verify the formation of Li metal on the Cu and $Ti_3C_2T_x$ substrates, the structure of the Li-$Ti_3C_2T_x$ and Li–Cu samples, together with that of commercial Li foil was analyzed by XRD (**Figure 5**a). The commercial Li metal showed a typical *bcc* structure. After depositing a certain amount of Li, two characteristic (110) and (200) peaks of *bcc*-Li were observed for both Li–Cu and Li-$Ti_3C_2T_x$. According to the above discussion, the *bcc*-Li was directly formed on the Cu foil. However, in the case of $Ti_3C_2T_x$, the deposited Li formed *hcp*-Li layers first and then followed by plating of *bcc*-Li. Unfortunately, it was difficult to distinguish *hcp*-Li from Li-$Ti_3C_2T_x$ because XRD is not a

powerful tool for detecting light elements, especially in a thin film form. One possible way to identify the *hcp*-Li layers in Li-$Ti_3C_2T_x$ is to use high-resolution TEM. Recently, Kühne et al. reported *hcp*-Li between two graphene sheets by in situ TEM.[32] Similar to $Ti_3C_2T_x$, graphene also has a hexagonal structure. Thus, it is reasonable to infer that the lattice confinement from the $Ti_3C_2T_x$ enabled the epitaxial deposition of *hcp*-Li layers. In an epitaxial electrodepostion process, a thin-film electrodeposit forms a coherent or semicoherent lattice interface with the substrate. The single crystalline new phase exhibits a correlated orientation in relation to the substrate and low residual stress.[10] Hence, it is suggested that 2D material with hexagonal surface structure is a prerequisite for the deposition of *hcp*-Li layers. However, other important factors, such as thermodynamic and thermal stability of the deposition system, as well as lattice matching between *hcp*-Li and the substrate must be considered. According to this conjecture, only a small number of substrates satisfy conditions for deposition of *hcp*-Li layers.
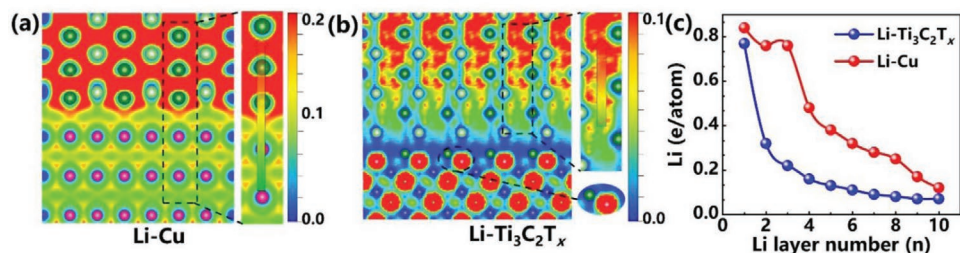

Figure 4. Electron density mapping of Li deposition on a) Cu and b) $Ti_3C_2T_x$. c) The charge transfer between Li and Cu and $Ti_3C_2T_x$ substrates as a function of number of deposition layers.
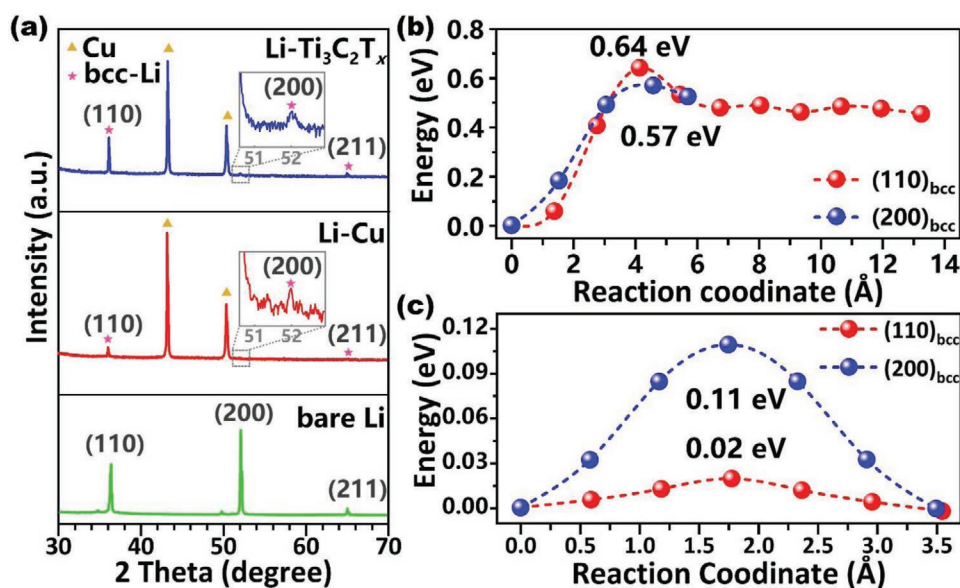
Figure 5. a) XRD patterns of the Li–Cu, Li-Ti$_3$C$_2$T$_x$@Cu and bare Li samples. b) Calculated dendrite formation energy and c) diffusion energy barriers of Li on the (110)$_{bcc}$ and (200)$_{bcc}$ surfaces.

With continuous deposition, the ionic interaction between Li and Ti$_3$C$_2$O$_2$ gradually decreased, which halted the formation of hcp-Li layers at $n = 9$. However, ab initio molecular dynamics (AIMD) simulations showed that only the hcp-Li layers near the surface of Ti$_3$C$_2$O$_2$ ($n < 4$) maintained structural stability at room temperature. Significant lattice distortion was observed above 4 hcp-Li layers due to the weak interaction between Li and Ti$_3$C$_2$O$_2$ (Figure S9, Supporting Information). This formed a transition region ($n = 4$–9) for the formation of hcp-Li which was thermodynamically allowed but thermally prohibited. Above this transition region, the Li deposition transformed to a nucleation process via Li−Li metallic bond (Figure S9f, Supporting Information).

The intensity ratio of the (110) and (200) peaks, $I_{110/200}$, was ≈21 for Li-Ti$_3$C$_2$T$_x$, which was much larger than that of ≈7 for Li−Cu. This suggested that Li grew along the (110)$_{bcc}$ facet on Ti$_3$C$_2$T$_x$, while it tended to grow along the (200)$_{bcc}$ facet on the Cu foil. Generally, the crystal facet that has smaller lattice mismatch (δ) with the substrate is more favorable for Li growth. As shown in Figure S10a, Supporting Information, the lattice of hcp-Li fit well with that of Ti$_3$C$_2$O$_2$ with ≈0% lattice mismatch. Thus, these hcp-Li layers built a perfect foundation for further deposition of bcc-Li. The lattice mismatch between (110)$_{bcc}$ and hcp-Li were 0.4% (δ_a) and 2.9% (δ_b) (Figure S10b, Supporting Information), which were much smaller than the 11.2% (δ_a) and 3.2% (δ_b) lattice mismatch between (200)$_{bcc}$ and hcp-Li (Figure S11a, Supporting Information). In contrast, the lattice mismatch between (200)$_{bcc}$ and Cu was 4.6% (Figures S10c, Supporting Information), much smaller than the 29.8% (δ_a) and 4.6% (δ_b) lattice mismatch between (110)$_{bcc}$ and Cu (Figure S11b, Supporting Information). Judged from these, it can be concluded that Li metal tended to grow along the (110)$_{bcc}$ facet on Ti$_3$C$_2$O$_2$, while it preferred to grow along the (200)$_{bcc}$ facet on the Cu foil which was consistent with the experimental result of the previous report.[33]

To study the probability of dendrite formation on the Cu and Ti$_3$C$_2$O$_2$ substrates, we calculated the dendrite formation energies

(E_{den}) of Li on the (200)$_{bcc}$ and (110)$_{bcc}$ surfaces. E_{den} is the difference in free energy (ΔG) between 1D (dendritic deposition) and 2D (planar deposition) Li. A higher E_{den} indicates formation of dendrites is more difficult and thus planar Li growth is expected. As shown in Figure 5b, the E_{den} of Li on the (200)$_{bcc}$ and (110)$_{bcc}$ surfaces were 0.57 and 0.64 eV, respectively. The larger E_{den} on the (110)$_{bcc}$ surface indicated that the Ti$_3$C$_2$O$_2$ substrate favored planar growth of Li. In addition, climbing-image nudged elastic band (CI-NEB) calculations showed the migration barriers of Li on the (110)$_{bcc}$ and (200)$_{bcc}$ surfaces were 0.02 and 0.11 eV, respectively (Figure 5c). The smaller migration barrier on (110)$_{bcc}$ indicated fast Li transport on this surface which resulted in the small deposition overpotential of the Li-Ti$_3$C$_2$T$_x$ electrode. Moreover, due to the faster migration on the (110)$_{bcc}$ surface, Li tended to deposit toward the nearby areas rather than on a lumped site, preventing the formation of dendrites.[11]

2.3. Electrochemical Performance of the Li Metal Electrodes

To evaluate the reversibility and efficiency of Li deposition on the Cu and Ti$_3$C$_2$T$_x$ substrates, Li‖Cu and Li‖Ti$_3$C$_2$T$_x$ half cells were assembled and the CEs of them were examined at a fixed areal capacity of 1.0 mA h cm^{-2}. As shown in **Figures 6**a–c, the one with Ti$_3$C$_2$T$_x$ substrate provided higher CEs and longer cycle life than that with Cu foil. At 0.5 and 1.0 mA cm^{-2} current densities, the CEs of Cu foil suddenly decreased after 250 and 90 cycles. In comparison, Ti$_3$C$_2$T$_x$ exhibited higher CEs of 98.4 and 98.0% under the same conditions, which could be maintained for hundreds of cycles. When the areal capacity increased to 2.0 mA h cm^{-2}, Ti$_3$C$_2$T$_x$ could still work for 300 cycles (Figure S12, Supporting Information). Compared with the Li metal anodes previously reported (Table S1, Supporting Information), the Ti$_3$C$_2$T$_x$ substrate exhibited longer cycle stability under normal current densities (<1.0 mA cm^{-2}). Moreover, the CEs could still be maintained at 90% for 160 cycles
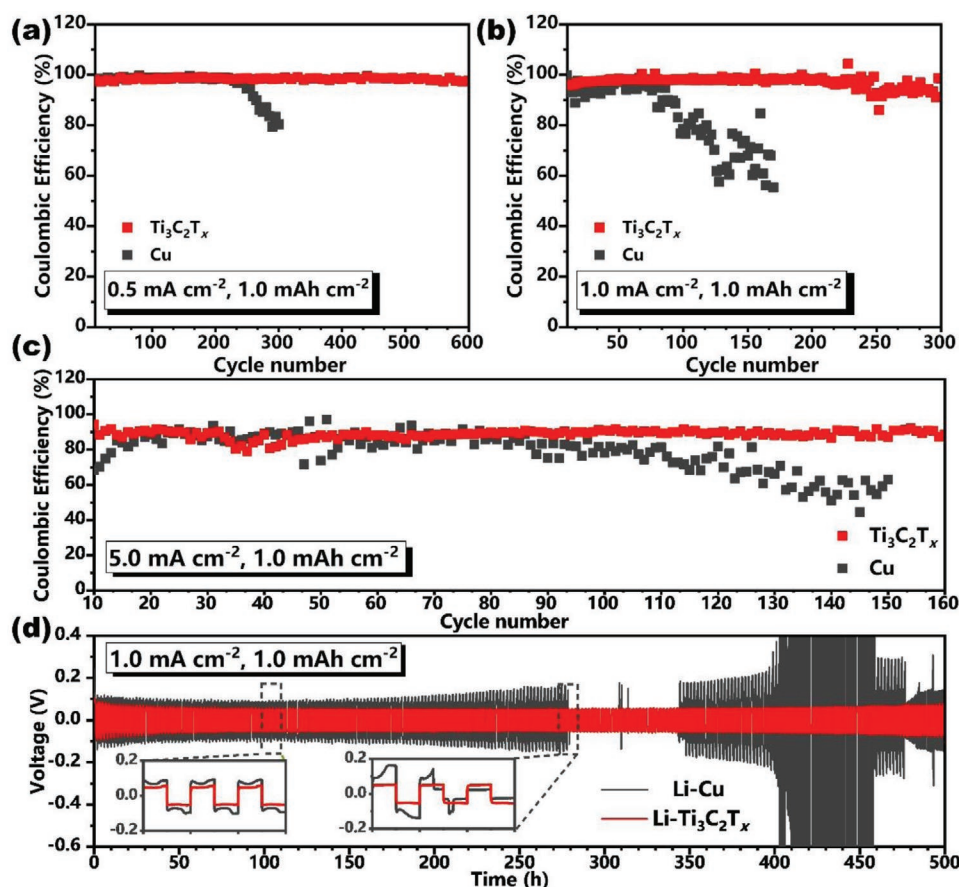
Figure 6. Electrochemical characterizations of the Cu and $Ti_3C_2T_x$ substrates. Coulombic efficiency of half-cells at the current density of a) 0.5, b) 1.0, and c) 5.0 mA cm^{-2}, the areal capacity of 1.0 mA h cm^{-2}. d) Charge–discharge curves of symmetric cells at 1.0 mA cm^{-2} current density.

at 5.0 mA cm^{-2}. In contrast, the initial CE of the Cu foil was only 79.0%, which decayed quickly after 90 cycles (Figure 6c). Additional experiments showed that the $Ti_3C_2T_x$ substrate could still achieve efficient Li deposition at a high current density of 10.0 mA cm^{-2} (Figure S13, Supporting Information). To further demonstrate the superiority of the $Ti_3C_2T_x$ substrate, we compared the polarization of the electrodes at the 5.0 mA cm^{-2} current density. The Li plating/stripping profiles of the Cu and $Ti_3C_2T_x$ substrates (Figure S14, Supporting Information) show insignificant polarization increase of the $Ti_3C_2T_x$ electrode with cycling, which was 85.3 and 89.9 mV at the 100th and 150th cycles, respectively. In comparison, the polarization of the Cu electrode increased from 298.6 to 525.5 mV. This indicates stable Li plating/stripping on the $Ti_3C_2T_x$ substrate, resulting in high CEs during long-term cycling.

Symmetrical cells were also assembled to study the electrochemical performance of the Li metal anodes. Obviously, Li-$Ti_3C_2T_x$ showed lower overpotential and more stable cycling (Figure 6d). At the 1.0 mA cm^{-2} current density and 1.0 mA h cm^{-2} deposition capacity, the Li-$Ti_3C_2T_x$ cell exhibited a stable overpotential of 54 mV over 500 h. Under the same conditions, the overpotential of Li–Cu was 75 mV during the first 200 h and then gradually increased, which indicated Li dendrites continuously formed on the electrode. Shortly afterwards, small internal short-circuit began to occur after 278 h, which indicated

the growing dendrites punctured the separator. To further understand the microscopic reasons for this performance of the Li-$Ti_3C_2T_x$ electrode, ex situ SEM experiments were carried out after 300 cycles. Dendrites can be clearly seen on the surface of the Li–Cu electrode (Figure 2e), while the surface of Li–$Ti_3C_2T_x$ was still flat and dense without noticeable dendrites (Figure 2k). Cross-sectional SEM images were also taken at the same time. As shown in Figure 2f,g, the thickness of the Li metal deposited on the Cu foil increased from ≈50 to ≈90 µm after 300 cycles, which was due to the porosity caused by dendritic growth. In comparison, the Li metal deposited on the $Ti_3C_2T_x$ substrate was still dense after 300 cycles, and its thickness only increased from ≈40 to ≈50 µm (Figure 2l,m). Combing these SEM observations, it can be concluded that the Li deposition on Cu foil continuously worsened with repeated charge–discharge, while the $Ti_3C_2T_x$ electrode could maintain dense and dendrite-free Li deposition during long-term cycling.

The performance of Li–$Ti_3C_2T_x$ and Li–Cu anodes in LMBs was examined using coin cells with a LiFePO$_4$ (LFP) cathode. Charge-discharge cycling at 0.2 C showed the Li-$Ti_3C_2T_x$‖LFP cell had better cycle stability than Li–Cu‖LFP did (Figure S15, Supporting Information). To examine the long-term cycle stability of the cells, charge-discharge experiments were performed at 1 C rate for 500 cycles. The Li–$Ti_3C_2T_x$‖LFP cell exhibited a discharge capacity of 135.2 mA h g^{-1}, with only
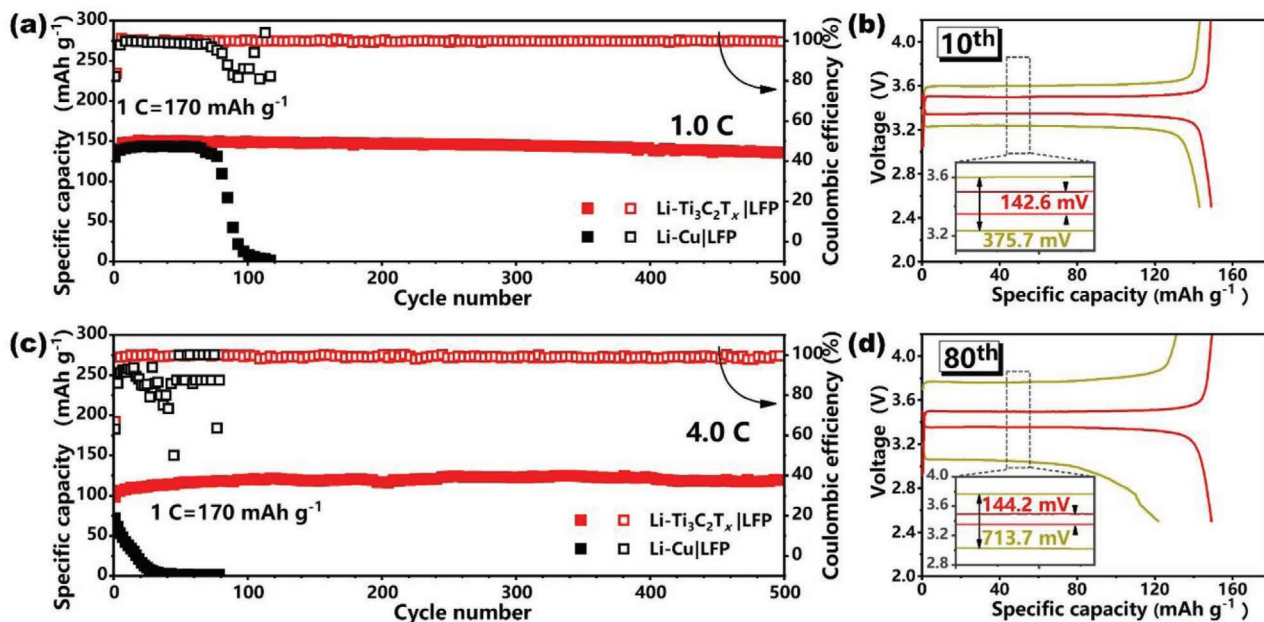
Figure 7. Charge-discharge performances of the Li-Ti$_3$C$_2$T$_x$|LFP and Li–Cu|LFP cells. Cycling performance at a) 1 C and c) 4 C rate. Charge–discharge curves of the b) 10th and d) 80th cycles at 1 C rate.

9.5% capacity fading after 500 cycles (**Figure 7**a). In comparison, the capacity of the Li–Cu‖LFP cell almost decreased to zero after 100 cycles. The possible reasons for the inferior cycling performance of Li–Cu‖LFP were studied with the help of charge-discharge profiles. The Li–Cu‖LFP cell showed severe electrode polarization even in the beginning of cycling. For example, the electrode polarization of 375.7 mV was observed at the 10th cycle, which was much larger than the 142.6 mV polarization of Li–Ti$_3$C$_2$T$_x$‖LFP (Figures 7b). Moreover, the polarization worsened fast with charge–discharge cycling, increasing to 713.7 mV after 80 cycles (Figure 7d). In comparison, the electrode polarization of Li–Ti$_3$C$_2$T$_x$‖LFP was almost unchanged (144.2 mV) during this process. Since the same LFP cathode was used in both cells, the different charge-discharge performances should be mainly attributed to the anodes. As observed in the SEM images, the Li–Ti$_3$C$_2$T$_x$ electrode stayed dense and flat during the cycling, while the Li–Cu electrode experienced a large volume expansion and serious side reactions during cycling, which inevitably led to the large polarization and poor cycling performance of Li–Cu‖LFP. To further evaluate the high-rate capability of the electrodes, charge-discharge cycling tests were performed at 4 C rate (Figure 7c). Even at such a high rate, the Li–Ti$_3$C$_2$T$_x$‖LFP cell could operate for 500 cycles with a specific capacity of about 120 mA h g^{-1}. This superior charge–discharge performance demonstrated the potential of the Ti$_3$C$_2$T$_x$ MXene substrate for high performance Li metal anodes.

3. Conclusions

Planar Li growth was achieved on a Ti$_3$C$_2$T$_x$ coated Cu foil substrate. Ab initio modeling suggests that, facilitated by the Ti$_3$C$_2$T$_x$ lattice confinement, hcp-Li layers first formed

on the Ti$_3$C$_2$T$_x$ surface via ionic bonding. With Li deposition increasing, the ionic bonding continuously weakened. This resulted in a transition layer of hcp-Li on MXene that was thermodynamically allowed but thermally prohibited. Above this transition layer, the deposition process was dominated by growth of bcc-Li with metallic bonding. Formation of dense and flat Li metal deposit was explained by the lattice matching between Ti$_3$C$_2$T$_x$ and hcp-Li and then bcc-Li, as well as the thermodynamically driven nucleation process. The prepared Li metal anode was nearly dendrite-free which resulted in high coulombic efficiency and long lifespan during high-rate charge-discharge cycling. The full cell fabricated with this Li metal anode showed stable cycling performance, highlighting the potential of Ti$_3$C$_2$T$_x$ MXene coated or freestanding MXene current collectors in Li metal batteries.

4. Experimental Section

Sample Preparation: For the preparation of Ti$_3$C$_2$T$_x$ MXene, Ti$_3$AlC$_2$ MAX phase was first prepared by mixing 7.368 g of Ti powder (Aladdin), 1.523 g of Al powder (Aladdin) and 1.109 g of graphite (Sigma-Aldrich) together, and then sintered at 1650 °C for 2 h under Ar atmosphere. The Ti$_3$C$_2$T$_x$ MXene was prepared by etching the Al layers from the Ti$_3$AlC$_2$ MAX phase. In detail, 1.6 g of LiF (Aladdin) was added into 20 mL of 9.0 M HCl under stirring.[27] Then 1.0 g of Ti$_3$AlC$_2$ powder was added to the solution and continuously reacted for 24 h at 30 °C. After that, the solution was centrifuged several times with deionized water at 8000 rpm to wash off the acidic mixture. The resulting slurry was sonicated for 10 min and centrifuged at 3500 rpm for 1 h to obtain a colloid supernatant solution containing Ti$_3$C$_2$T$_x$ nanosheets. Finally, the powder containing Ti$_3$C$_2$T$_x$ nanosheets was obtained after vacuum freeze drying.

To prepare the Ti$_3$C$_2$T$_x$ substrate, a commercial Cu foil current collector (Shenzhen Biyuan Electronics Co., Ltd.) used for Li ion batteries was treated with ethanol repeatedly to remove surface impurities. After that, the Ti$_3$C$_2$T$_x$ nanosheets powder was blended with poly-vinylidene

fluoride (PVDF, Sigma-Aldrich) in a mass ratio of 9:1, mixed with a N-methyl pyrrolidone (NMP, Sigma-Aldrich) solvent and grinded for 30 min to form a uniform slurry. Then, the slurry was casted onto the Cu foil using a doctor blade and vacuum dried at 60 °C for 6 h. The obtained $Ti_3C_2T_x$ substrate was cut into squares of 0.8×0.8 cm^2 size for use.

Structural and Morphological Characterizations: X-ray diffraction (XRD) experiments were performed on a Bruker AXS D8 X-ray diffractometer with Cu K$_\alpha$ radiation. The morphology of the substrates was studied by using a JEOL JSM-7900F scanning electron microscope (SEM) with operation voltage of 5.0 kV. The microstructures of the substrates were characterized by a JEOL JEM-2200FS transmission electron microscope (TEM) operated at 200 kV. The thickness of the $Ti_3C_2T_x$ nanosheets and the surface roughness of the substrates were determined by a CSPM 5500 atomic force microscope (AFM). For characterization of Li metal electrodes, the cells were disassembled in an Ar-filled glove box and then the Li electrodes were sealed in an Ar-filled container to isolate air contact during test and sample transportation.

Electrochemical Experiments: CR2032 coin cells were assembled in an Ar-filled glove box with oxygen and water contents below 0.1 ppm. A LAND-2100 automatic battery tester was used for electrochemical testing. For coulombic efficiency (CE) tests, the Cu or $Ti_3C_2T_x$ substrate was used as the working electrode, and Li foil as the counter electrode, with 1 M lithium bis(trifluoromethane sulfonyl)imide (LiTFSI) dissolved in 1, 3-dioxolane (DOL) and 1, 2-dimethoxyethane (DME), 1:1 by volume ratio with 2.0 wt% LiNO$_3$ additive as the electrolyte. The cells were first activated in 0–1.0 V (vs Li$^+$/Li) for 5 cycles, and then discharged at different current densities to deposit a fixed amount of Li on the working electrode, and stripped Li until the charging voltage reached 1.0 V (vs Li$^+$/Li). To obtain Li–Cu and Li-$Ti_3C_2T_x$ electrodes, the cells were first discharged to 0.1 V, and then electrodeposition experiments were performed by controlling the current density and deposition time. For symmetrical cell tests, the cathode and anode were both made of either Li-$Ti_3C_2T_x$ or Li–Cu electrodes. A current density of 1.0 mA cm^{-2} and areal capacity of 1.0 mA h cm^{-2} were used for galvanostatic cycling. The full battery cells were assembled using the Li–$Ti_3C_2T_x$ or Li–Cu electrode as the anode, Celgard 2400 as the separator, and LiFePO$_4$ as the cathode. The LiFePO$_4$ powder was mixed with PVDF binder and Super P conductive additive in a weight ratio of 8:1:1. The mass loading of LiFePO$_4$ in the electrode was 1.3 mg cm^{-2}. Each coin cell contained around 80 µL electrolyte. The cells were galvanostatically cycled between 2.5 and 4.2 V. The rest of the above electrochemical experiments all used a 1.0 M LiPF$_6$ electrolyte dissolved in a 1:1 (volume ratio) EC/DEC solvent.

First-Principles Calculations: All the first-principles calculations were performed in the framework of density functional theory (DFT), as implemented in the Vienna ab initio simulation package (VASP).[34] The projector augmented wave[35] (PAW) potential was used with a plane-wave cutoff energy of 550 eV. The exchange correlation energy was described by the generalized gradient approximation (GGA) in the scheme proposed by Perdew-Burke-Ernzerhof (PBE).[36] Pseudo-potentials utilized the valence state of $2s^1 2p^0$ for Li, $3d^2 4s^2$ for Ti, $2s^2 2p^4$ for O, $2s^2 2p^2$ for C, and $3d^{10} 4s^1$ for Cu. For geometry optimization, the Brillouin-zone integration was performed using a $7 \times 7 \times 1$ Monkhorst–Pack grid of Brillouin-zone k-point sampling. To avoid any interactions due to the use of periodic boundary conditions, a vacuum separation between two neighboring cells was set to >20 Å. Geometry optimizations were performed using the conjugated gradient method, and the convergence threshold was set at 10^{-6} eV atom^{-1} in energy and 0.01 eV Å^{-1} in force. The stability of different Li deposition configurations was determined by simulating the Li deposition process on different substrates and calculating the corresponding adsorption energy values. In addition, the charge transfer between Li and each substrate was studied by Bader charge analysis, which helped to understand the Li deposition mechanism on different substrates. To simulate the adsorption and diffusion of Li on $Ti_3C_2T_x$ and Cu substrates, a $5 \times 5 \times 1$ supercell was used. To accurately deal with the van der Waals (vdW) forces between Li and the $Ti_3C_2T_x$ or Cu substrates, a newly developed vdW-inclusive DFT-D3

method was incorporated in the calculations.[37] Moreover, the climbing-image nudged elastic band (CI-NEB) method was used to calculate the dendrite formation energy.[38] Herein, eight images for $Ti_3C_2T_x$ and five images for Cu including the initial and final positions (before and after dendrite formation, respectively) were simulated for CI-NEB calculations. The energy difference between these images (saddle point) and the initial image was defined as the dendrite formation energy barrier. Meanwhile, the migration barriers of Li on the $(110)_{bcc}$ and $(200)_{bcc}$ surfaces of Li metal were calculated by the CI-NEB method. Ab initio molecular dynamics (AIMD) simulations for $5 \times 5 \times 1$ supercells were performed at 300K. AIMD simulation in the NVT ensemble lasted 5 ps with a time step of 1.0 fs. The temperature was controlled using the Nosé–Hoover method.

Supporting Information

Supporting Information is available from the Wiley Online Library or from the author.

Conflict of Interest

The authors declare no conflict of interest.

Data Availability Statement

The data that support the findings of this study are available from the corresponding author upon reasonable request.

[1] S. Li, M. Jiang, Y. Xie, H. Xu, J. Jia, J. Li, *Adv. Mater.* **2018**, *30*, 1706375.

[2] a) D. Lin, Y. Liu, Y. Cui, *Nat. Nanotechnol.* **2017**, *12*, 194; b) X.-Q. Zhang, X.-B. Cheng, Q. Zhang, *Adv. Energy Mater.* **2018**, *5*, 1701097; c) B. Li, Y. Wang, S. Yang, *Adv. Energy Mater.* **2018**, *8*, 1702296.

[3] T. T. Zuo, Y. X. Yin, S. H. Wang, P. F. Wang, X. Yang, J. Liu, C. P. Yang, Y. G. Guo, *Nano Lett.* **2018**, *18*, 297.

[4] a) Q. Li, S. Zhu, Y. Lu, *Adv. Funct. Mater.* **2017**, *27*, 1606422; b) K. N. Wood, M. Noked, N. P. Dasgupta, *ACS Energy Lett.* **2017**, *2*, 664.

[5] S. H. Wang, Y. X. Yin, T. T. Zuo, W. Dong, J. Y. Li, J. L. Shi, C. H. Zhang, N. W. Li, C. J. Li, Y. G. Guo, *Adv. Mater.* **2017**, *29*, 1703729.

[6] X. Xu, S. Wang, H. Wang, C. Hu, Y. Jin, J. Liu, H. Yan, *J. Energy Chem.* **2018**, *27*, 513.

[7] a) H. Qiu, T. Tang, M. Asif, X. Huang, Y. Hou, *Adv. Funct. Mater.* **2019**, *29*, 1808468; b) H. Zhao, D. Lei, Y.-B. He, Y. Yuan, Q. Qun, B. Ni, W. Lv, B. Li, Q.-H. Yang, F. Kang, J. Lu, *Adv. Energy Mater.* **2018**, *8*, 1800266; c) C. Zhang, W. Lv, G. Zhou, Z. Huang, Y. Zhang, R. Lyu, H. Wu, Q. Yun, F. Kang, Q.-H. Yang, *Adv. Energy Mater.* **2018**, *8*, 1703404; d) Q. Yun, Y. B. He, W. Lv, Y. Zhao, B. Li, F. Kang, Q. H. Yang, *Adv. Mater.* **2016**, *28*, 6932; e) D. Lin, Y. Liu, Z. Liang, H. W. Lee, J. Sun, H. Wang, K. Yan, J. Xie, Y. Cui, *Nat. Nanotechnol.* **2016**, *11*, 626; f) L. L. Lu, J. Ge, J. N. Yang, S. M. Chen, H. B. Yao, F. Zhou, S. H. Yu, *Nano Lett.* **2016**, *16*, 4431; g) B. Zhang, H. Shi, Z. Ju, K. Huang, C. Lian, Y. Wang, O. Sheng, J. Zheng, J. Nai, T. Liu, Y. Jin, Y. Liu, C. Zhang, X. Tao, *J. Mater. Chem. A* **2020**, *8*, 26045.

[8] C. P. Yang, Y. X. Yin, S. F. Zhang, N. W. Li, Y. G. Guo, *Nat. Commun.* **2015**, *6*, 8058.

[9] K. Yan, Z. Lu, H.-W. Lee, F. Xiong, P.-C. Hsu, Y. Li, J. Zhao, S. Chu, Y. Cui, *Nat. Energy* **2016**, *1*, 16010.

[10] J. Zheng, Q. Zhao, T. Tang, J. Yin, C. D. Quilty, G. D. Renderos, X. Liu, Y. Deng, L. Wang, D. C. Bock, C. Jaye, D. Zhang, E. S. Takeuchi, K. J. Takeuchi, A. C. Marschilok, L. A. Archer, *Science* **2019**, *366*, 645.

[11] X. B. Cheng, R. Zhang, C. Z. Zhao, Q. Zhang, *Chem. Rev.* **2017**, *117*, 10403.

[12] S. Liu, X. Zhang, R. Li, L. Gao, J. Luo, *Energy Storage Mater.* **2018**, *14*, 143.

[13] A. J. Sanchez, E. Kazyak, Y. Chen, K.-H. Chen, E. R. Pattison, N. P. Dasgupta, *ACS Energy Lett.* **2020**, *5*, 994.

[14] R. Zhang, X. R. Chen, X. Chen, X. B. Cheng, X. Q. Zhang, C. Yan, Q. Zhang, *Angew. Chem., Int. Ed.* **2017**, *56*, 7764.

[15] K. Yan, H. W. Lee, T. Gao, G. Zheng, H. Yao, H. Wang, Z. Lu, Y. Zhou, Z. Liang, Z. Liu, S. Chu, Y. Cui, *Nano Lett.* **2014**, *14*, 6016.

[16] C. Wei, Y. Tao, Y. An, Y. Tian, Y. Zhang, J. Feng, Y. Qian, *Adv. Funct. Mater.* **2020**, *30*, 2004613.

[17] a) C. Zhang, Y. Ma, X. Zhang, S. Abdolhosseinzadeh, H. Sheng, W. Lan, A. Pakdel, J. Heier, F. Nüesch, *Energy Environ. Mater.* **2020**, *3*, 29; b) S. Abdolhosseinzadeh, R. Schneider, A. Verma, J. Heier, F. Nuesch, C. J. Zhang, *Adv. Mater.* **2020**, *32*, 2000716; c) C. Zhang, L. Cui, S. Abdolhosseinzadeh, J. Heier, *InfoMat* **2020**, *2*, 613.

[18] J. Zhang, N. Kong, S. Uzun, A. Levitt, S. Seyedin, P. A. Lynch, S. Qin, M. Han, W. Yang, J. Liu, X. Wang, Y. Gogotsi, J. M. Razal, *Adv. Mater.* **2020**, *32*, 2001093.

[19] X. Zhang, R. Lv, A. Wang, W. Guo, X. Liu, J. Luo, *Angew. Chem., Int. Ed.* **2018**, *57*, 15028.

[20] H. Shi, C. J. Zhang, P. Lu, Y. Dong, P. Wen, Z. S. Wu, *ACS Nano* **2019**, *13*, 14308.

[21] H. Shi, M. Yue, C. J. Zhang, Y. Dong, P. Lu, S. Zheng, H. Huang, J. Chen, P. Wen, Z. Xu, Q. Zheng, X. Li, Y. Yu, Z. S. Wu, *ACS Nano* **2020**, *14*, 8678.

[22] Y. Fang, Y. Zhang, K. Zhu, R. Lian, Y. Gao, J. Yin, K. Ye, K. Cheng, J. Yan, G. Wang, Y. Wei, D. Cao, *ACS Nano* **2019**, *13*, 14319.

[23] J. Luo, C. Wang, H. Wang, X. Hu, E. Matios, X. Lu, W. Zhang, X. Tao, W. Li, *Adv. Funct. Mater.* **2019**, *29*, 1805946.

[24] D. Zhang, S. Wang, B. Li, Y. Gong, S. Yang, *Adv. Mater.* **2019**, *31*, 1901820.

[25] Y. Fang, R. Lian, H. Li, Y. Zhang, Z. Gong, K. Zhu, K. Ye, J. Yan, G. Wang, Y. Gao, Y. Wei, D. Cao, *ACS Nano* **2020**, *14*, 8744.

[26] Q. Yan, G. Whang, Z. Wei, S.-T. Ko, P. Sautet, S. H. Tolbert, B. S. Dunn, J. Luo, *Appl. Phys. Lett.* **2020**, *117*, 080504.

[27] M. Alhabeb, K. Maleski, B. Anasori, P. Lelyukh, L. Clark, S. Sin, Y. Gogotsi, *Chem. Mater.* **2017**, *29*, 7633.

[28] M. S. Kim, J.-H. Ryu, Deepika, Y. R. L. , I. W. Nah, K.-R. Lee, L. A. Archer, W. Il Cho, *Nat. Energy* **2018**, *3*, 889.

[29] A. Pei, G. Zheng, F. Shi, Y. Li, Y. Cui, *Nano Lett.* **2017**, *17*, 1132.

[30] Y. Xie, M. Naguib, V. N. Mochalin, M. W. Barsoum, Y. Gogotsi, X. Yu, K. W. Nam, X. Q. Yang, A. I. Kolesnikov, P. R. Kent, *J. Am. Chem. Soc.* **2014**, *136*, 6385.

[31] B. Anasori, Y. Gogotsi, *2D Metal Carbides and Nitrides (MXenes) Structure, Properties and Applications*, Springer Nature, Switzerland **2019**.

[32] M. Kuhne, F. Borrnert, S. Fecher, M. Ghorbani-Asl, J. Biskupek, D. Samuelis, A. V. Krasheninnikov, U. Kaiser, J. H. Smet, *Nature* **2018**, *564*, 234.

[33] N. Li, K. Zhang, K. Xie, W. Wei, Y. Gao, M. Bai, Y. Gao, Q. Hou, C. Shen, Z. Xia, B. Wei, *Adv. Mater.* **2019**, *23*, 1907079.

[34] G. Kresse, J. Furthmuller, *Phys. Rev. B* **1996**, *54*, 11169.

[35] G. Kresse, D. Joubert, *Phys. Rev. B* **1998**, *59*, 1758.

[36] J. P. Perdew, K. Burke, M. Ernzerhof, *Phys. Rev. Lett.* **1996**, *77*, 3865.

[37] S. Grimme, J. Antony, S. Ehrlich, H. Krieg, *J. Chem. Phys.* **2010**, *132*, 154104.

[38] G. Henkelman, B. P. Uberuaga, H. Jónsson, *J. Chem. Phys.* **2000**, *113*, 9901.